

The zonal equatorial wind switch of IOD variability: Lessons from a simple reduced-gravity modelling study

Jochen Kaempf¹

¹Flinders University

March 9, 2023

Abstract

Using a reduced-gravity model, this study explores the ocean's response to wind forcing in the South-East Tropical Indian Ocean (SETIO) during the development phase (July-September) of positive phases of the Indian Ocean Dipole (IOD), using the years of 2009 and 2019 for comparison. Findings show that IOD variability is exclusively controlled by zonal equatorial wind anomalies. In the average situation, represented by the 2009 season, westerly equatorial winds create downwelling Kelvin waves that operate to suppress the Sumatran upwelling. In contrast, positive phases of the IOD, represented by the 2019 season, are characterized by easterly equatorial winds that reverse the equatorial influence, which leads to strong coastal upwelling off Sumatra's southeast coast. In addition, findings show that the Sumatran upwelling involves the formation of a strong northwestward surface flow, the South-East Sumatra Current, that transports colder seawater into the region, which contributes to the IOD anomaly.

Hosted file

957715_0_art_file_10766007_rqz6rs.docx available at <https://authorea.com/users/529750/articles/628263-the-zonal-equatorial-wind-switch-of-iod-variability-lessons-from-a-simple-reduced-gravity-modelling-study>

1
2
3
4
5
6
7
8
9
10
11
12

The zonal equatorial wind switch of IOD variability: Lessons from a simple reduced-gravity modelling study

J. Kämpf¹

¹College of Science and Engineering, Flinders University, Adelaide, Australia

Corresponding author: Jochen Kämpf (jochen.kaempf@flinders.edu.au)

Key Points:

- Uses a reduced-gravity model to study the ocean's response to wind forcing in the southeast tropical Indian Ocean
- Shows that equatorial wind is an exclusive control of the development of positive phases of the Indian Ocean Dipole
- Explains this by a Kelvin-wave response to equatorial perturbations of the thermocline

13 **Abstract**

14 Using a reduced-gravity model, this study explores the ocean's response to wind forcing in the
15 South-East Tropical Indian Ocean (SETIO) during the development phase (July-September) of
16 positive phases of the Indian Ocean Dipole (IOD), using the years of 2009 and 2019 for
17 comparison. Findings show that IOD variability is exclusively controlled by zonal equatorial
18 wind anomalies. In the average situation, represented by the 2009 season, westerly equatorial
19 winds create downwelling Kelvin waves that operate to suppress the Sumatran upwelling. In
20 contrast, positive phases of the IOD, represented by the 2019 season, are characterized by
21 easterly equatorial winds that reverse the equatorial influence, which leads to strong coastal
22 upwelling off Sumatra's southeast coast. In addition, findings show that the Sumatran upwelling
23 involves the formation of a strong northwestward surface flow, the South-East Sumatra Current,
24 that transports colder seawater into the region, which contributes to the IOD anomaly.

25

26 **Plain Language Summary**

27 The Indian Ocean Dipole (IOD) is a mode of natural year-to-year climate variability that strongly
28 influences rainfall extremes in countries bordering the Indian Ocean. The positive phase of the
29 IOD is characterized by the cooling of surface waters off Sumatra's southwest coast. This study
30 uses a simplified computer model to explore the ocean's response to wind forcing characterizing
31 different phases of the IOD. Findings reveal that the ocean's response exclusively depends on the
32 direction of equatorial wind in the eastern Indian Ocean. The wind direction determines whether
33 the surface layer of the ocean shoals or deepens along the equator, leading to a Kelvin wave
34 disturbance that either enhances or suppresses the appearance of cold surface water off
35 Sumatra's southwest coast. Concludingly, the direction of equatorial wind appears as a principal
36 driver of IOD variability.

37

38 1 Introduction

39 The Indian Ocean Dipole (IOD) is a coupled atmosphere-ocean mode of interdecadal
40 climate variability that strongly affects rainfall variability and extremes in countries bordering
41 the Indian ocean (e.g., Saji and Yamagata, 2003; Behera et al., 2005; Chan et al., 2008; Cai et al.,
42 2009; Qiu et al., 2014). Improved forecasting of IOD variability and how this variability will
43 change under the global warming scenario has a high research priority in the climate sciences.

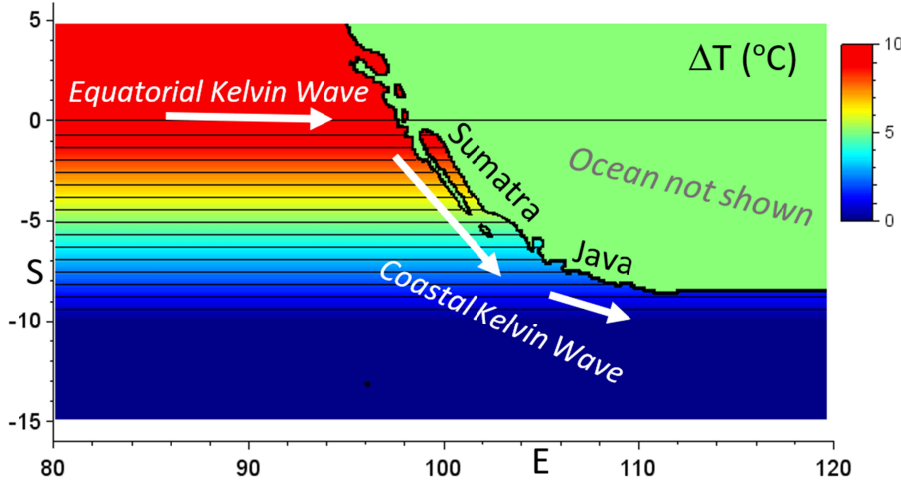
44 The IOD, first described by Saji et al. (1999), is a pattern of sea surface temperature
45 (SST) fluctuations between the eastern and western intertropical Indian Ocean that can be
46 characterized by the difference in SSTs of defined areas, called the Dipole Mode Index (DMI).
47 Positive phases of the IOD, called pIOD events, are dominated by the widespread cooling of the
48 surface ocean off Sumatra's southwest coast. SST anomalies tend to peak in late austral winter
49 and spring (August to November) (Kämpf and Kavi, 2019). pIOD events are traditionally
50 defined by DMI values exceeding 1°C for a period exceeding 12 weeks. After this definition,
51 only four significant cooling events occurred in the years 1994, 1997, 2006 and 2019 since 1988
52 (see Kämpf and Kavi 2019). Hence, the occurrence of pronounced pIOD events is relatively rare.

53 The development of pIOD events is often explained by the Bjerknes feedback (Bjerknes,
54 1966, 1969), wherein an initial cooling off the coast of Sumatra–Java suppresses local
55 atmospheric convection, leading to anomalous easterly wind, a shoaling thermocline and
56 stronger upwelling which in turn reinforce the initial cooling (Saji et al. 1999; Webster et al.
57 1999; Feng and Meyers 2003; Cai et al. 2014, 2018). Lu and Ren (2020) suggested that a record-
58 breaking interhemispheric sea-level pressure gradient between Australia and the South China
59 Sea/Philippine Sea forming from May 2019 induced anomalously strong southeasterlies along
60 Sumatra's coast as a cause of the subsequent pIOD event through the Bjerknes feedback.

61 Kämpf and Kavi (2019) presented an analytical theory of wind-driven upwelling along a
62 coastline of finite length based on Kelvin-wave propagation. This theory suggests that wind-
63 driven coastal Kelvin waves initiated near the equator can strongly modify the Sumatran
64 upwelling. Analytical results derived from this theory were consistent with the statistics of pIOD
65 events. It should be noted that the theory did not account for the effects of zonal equatorial wind
66 anomalies. Kämpf and Kavi (2019) also analyzed the surface dynamic height field characteristic
67 of pIOD events. This analysis infers the formation of a northwestward geostrophic surface flow,
68 called the South-West Sumatra Current (SWSC), that has the potential to transport colder water
69 into the region.

70 Kavi and Kämpf (2022) reported the existence of short-lived atmospheric cyclones in the
71 South-Eastern Tropical Indian Ocean (SETIO), referred to as SETIO cyclones, comprising
72 westerly equatorial wind bursts and northwesterly wind anomalies along Sumatra's coast.
73 Findings indicate that SETIO cyclones operate to weaken the Sumatran upwelling, and that
74 pIOD events follow from the relative absence of SETIO cyclones that intensifies southeasterlies
75 along Sumatra's coast. Interestingly, the formation of SETIO cyclones commences with westerly
76 equatorial wind bursts, which is like the Pacific situation, where such wind bursts lead to the
77 suppressing of the Peru upwelling in El-Niño events (e.g., McPhaden 1999). It should be
78 highlighted that SETIO cyclones already start to form in early austral winter from July, which
79 precedes the timing of SST anomalies of pIOD events by 1-2 months (see Kavi and Kämpf,
80 2022).

81 Equatorial zonal wind induces coastal upwelling or downwelling off Sumatra's west
 82 coast through the so-called lee effect (Hela 1976, Kämpf 2015). Equatorial wind also induces
 83 upwelling or downwelling through the horizontal flow divergence it creates. The resulting
 84 thermocline disturbances can only propagate eastward along the equator in the form of an
 85 equatorial Kelvin Wave and southeastward along Sumatra's coast as a coastal Kelvin wave
 86 (**Figure 1**).



87

88 **Figure 1:** Model domain showing the initial distribution of an Eulerian tracer field, ΔT
 89 ($^{\circ}\text{C}$), that mimics the temperature field of the south-eastern tropical Indian Ocean. Arrows
 90 illustrate the propagation direction of equatorial and coastal Kelvin waves.

91 This paper uses a simple reduced-gravity model to explore the ocean's response to wind
 92 fields of two selected years that characterize the onset period (July-September) of different
 93 phases of the IOD. The underlying research question addressed is whether equatorial winds,
 94 coastal winds or both are responsible for the creation of positive IOD events.

95 2 Methodology

96 2.1 Model description

97 This work applies a reduced gravity-model being cast in a Cartesian coordinate system using the
 98 equatorial beta-plane approximation of the Coriolis parameter. This reduced-gravity model does
 99 not account for air-sea density fluxes or horizontal density changes. Frictional effects at the base
 100 of the surface mixed layer are also ignored. This model is governed by the equations:

$$101 \quad \frac{\partial}{\partial t} \mathbf{u} + \mathbf{u} \frac{\partial}{\partial x} \mathbf{u} + \mathbf{v} \frac{\partial}{\partial y} \mathbf{u} - f\mathbf{v} = \frac{\Delta p}{\rho_0} \mathbf{g} \frac{\partial}{\partial x} \mathbf{h} + \frac{\tau_x}{\rho_0} + \frac{\partial}{\partial x} \left(A_h \frac{\partial}{\partial x} \mathbf{u} \right) + \frac{\partial}{\partial y} \left(A_h \frac{\partial}{\partial y} \mathbf{u} \right) \quad (1)$$

$$102 \quad \frac{\partial}{\partial t} \mathbf{v} + \mathbf{u} \frac{\partial}{\partial x} \mathbf{v} + \mathbf{v} \frac{\partial}{\partial y} \mathbf{v} + f\mathbf{u} = \frac{\Delta p}{\rho_0} \mathbf{g} \frac{\partial}{\partial y} \mathbf{h} + \frac{\tau_y}{\rho_0} + \frac{\partial}{\partial x} \left(A_h \frac{\partial}{\partial x} \mathbf{v} \right) + \frac{\partial}{\partial y} \left(A_h \frac{\partial}{\partial y} \mathbf{v} \right) \quad (2)$$

$$103 \quad \frac{\partial}{\partial t} \mathbf{h} + \frac{\partial}{\partial x} (\mathbf{h}\mathbf{u}) + \frac{\partial}{\partial y} (\mathbf{h}\mathbf{v}) = 0 \quad (3)$$

104 where (x,y) are horizontal coordinates with $y = 0$ marking the equator, (u,v) is horizontal

105 velocity, the Coriolis parameter is approximated as $f = \beta y$ with $\beta = 2.2 \times 10^{-11} \text{ s}^{-1} \text{ m}^{-1}$, $\Delta\rho$ is the
 106 seawater density anomaly of the surface mixed layer, $\rho_0 = 1026 \text{ kg m}^{-3}$ is the ambient seawater
 107 density, h is the thickness of the surface mixed layer, (τ_x, τ_y) is the wind-stress vector, and A_h is
 108 horizontal diffusivity, set to a constant value of $1000 \text{ m}^2/\text{s}$. Variation of A_h did not significantly
 109 alter the results. Results are expressed in terms of thermocline displacements, given by $\eta^* = h -$
 110 h_0 , where $h_0 = 100 \text{ m}$ is the initial thickness of the surface mixed layer.

111 Using the latest GEBCO bathymetry available on a 15 arc-second interval grid, the model
 112 equations are applied with a grid resolution of $\Delta x = \Delta y = 13,750 \text{ m}$ to the study region covering
 113 geographical longitudes from 80° to 120°E and latitudes from 15°S to 5°N (see Fig. 1), which is
 114 larger than the region ($90\text{--}110^\circ\text{E}$, $10\text{--}0^\circ\text{S}$) used to calculate the DMI. For simplicity, passages of
 115 the Indonesian Throughflow including Lombok Strait and Ombai Strait are closed, and oceans on
 116 the other side of these passages are ignored in the simulations. The minimum water depth is set
 117 to 500 m , exceeding the maximum thickness of the surface mixed layer. The initial thickness of
 118 the surface mixed layer is set to 100 m throughout the model domain. The density anomaly of the
 119 surface mixed layer is set to 5 kg/m^3 , which is sufficient to prevent outcropping of the
 120 thermocline during simulations. Wind stresses are calculated from wind speeds at 10-m above
 121 sea level using standard bulk formulae with a wind drag coefficient of 1.2×10^{-3} . Zero-gradient
 122 conditions are used along all open boundaries. In addition, Rayleigh-damping conditions are
 123 applied to interface displacements near the northern, southern, and eastern open boundaries. In
 124 these zones, the Rayleigh damping coefficient increases from zero to a maximum value of 0.01
 125 over 10 grid points from a boundary.

126 An advection-diffusion equation is used to predict the deformation of a Eulerian tracer
 127 field, ΔT , approximating temperatures anomalies of the surface ocean. This equation is given by:

$$128 \quad \frac{\partial}{\partial t} \Delta T + \mathbf{u} \frac{\partial}{\partial x} \Delta T + \mathbf{v} \frac{\partial}{\partial y} \Delta T = \frac{\partial}{\partial x} \left(K_h \frac{\partial}{\partial x} \Delta T \right) + \frac{\partial}{\partial y} \left(K_h \frac{\partial}{\partial y} \Delta T \right) \quad (4)$$

129 where K_h is also set to $1000 \text{ m}^2 \text{ s}^{-1}$. Initially, ΔT increases linearly by 10°C from 10°S to the
 130 equator (see Figure 1), which is based on observed temperature scales. Kämpf (2009) describes
 131 the numerical treatment of (1) to (4), noting that a no-slip condition is used for the flow
 132 component parallel to a coastline.

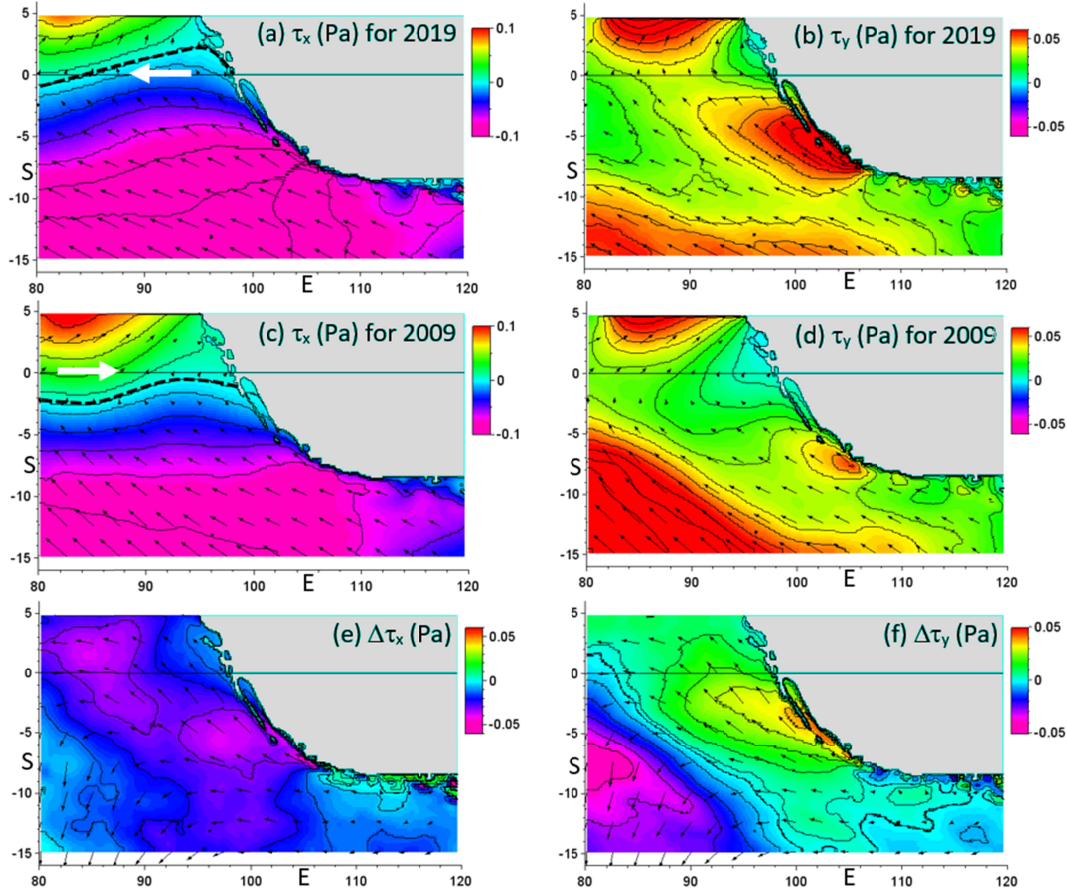
133 2.2 Experimental design

134 The model is forced by daily CCMP v2.0 wind data averaged over the period July-
 135 September, corresponding to the development phase of IOD events (see Kämpf and Kavi, 2019).
 136 The use of daily wind data without averaging yielded similar results (not shown). The focus is
 137 placed on the contrasting seasons of two years, namely 2019 and 2009, that characterize opposite
 138 phased of the IOD. A particularly strong pIOD developed during this period in 2019 (see Lu and
 139 Ren, 2020), whereas 2009 characterizes the neutral phase of the IOD (see Kämpf and Kavi,
 140 2019). The static, but spatially variable wind fields are linearly adjusted from zero to their final
 141 values over the first 5 simulation days to avoid the generation of unwanted dynamical
 142 disturbances. Using a numerical timestep of 120 s , the total simulation time of experiments is 60
 143 days (2 months).

144 For comparison, the model simulations for both 2009 and 2019 seasons are repeated with
 145 the addition of Rayleigh-damping of interface displacements in a zone centered over the equator.
 146 The damping is of the form of:

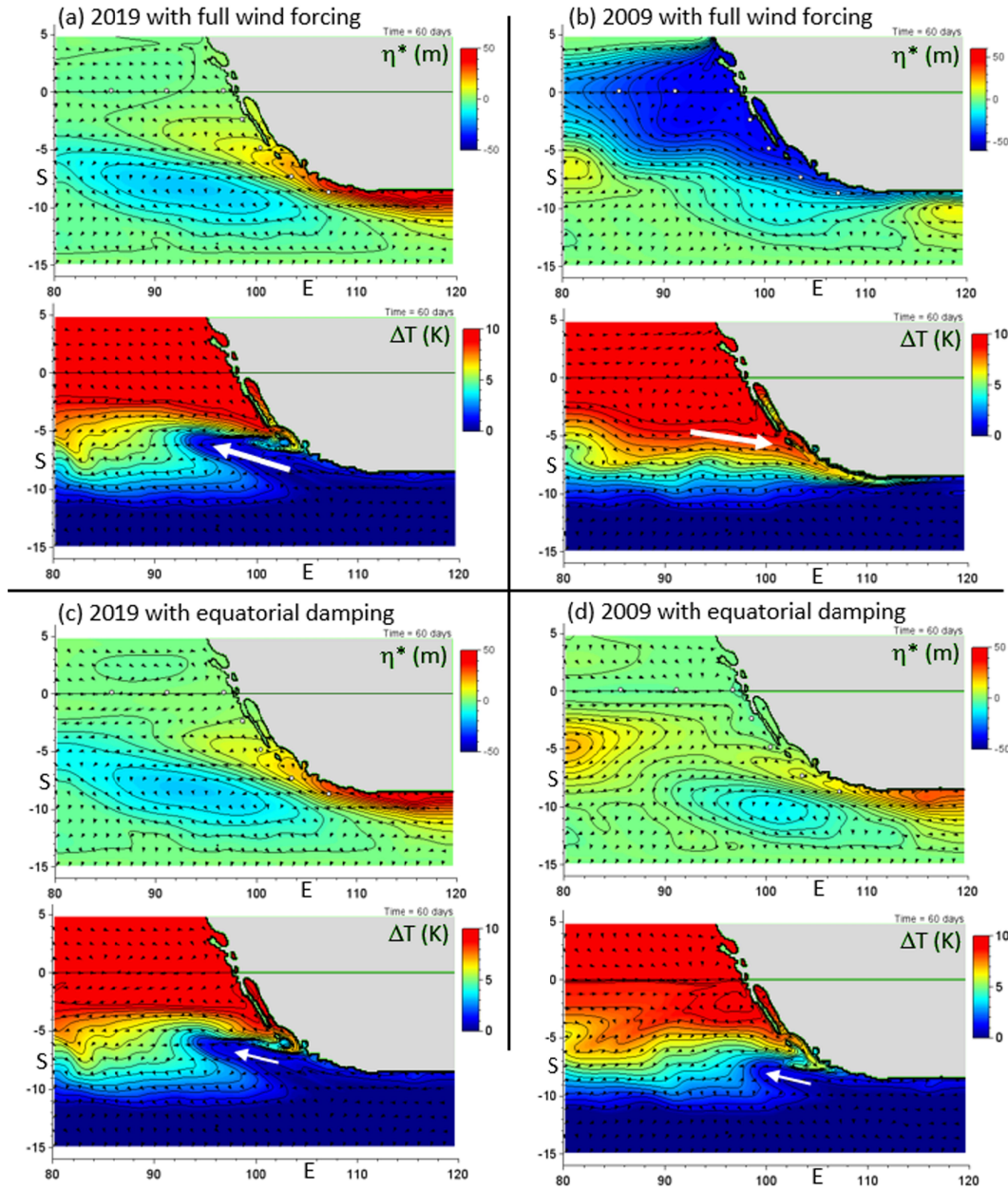
$$147 \quad \frac{\partial}{\partial t} \eta^* = -\varepsilon \eta^* \quad (5)$$

148 where $\varepsilon = 0.001 \max(1 - |y|/y^*, 0)$ with $y^* = 200$ km. This approach allows to indirectly quantify
 149 the role that equatorial winds play in the development of pIOD events.



150

151 **Figure 2:** Horizontal distribution of the zonal and meridional components of wind stress (τ_x , τ_y)
 152 for the July-September periods of 2019, shown in panels a) and b), and 2009, shown in panels c)
 153 and d). Panels e) and f) display the anomaly maps of 2019 minus 2009 wind components. CI =
 154 0.02 Pa in all panels. Arrows are horizontal wind vectors; only every 20th vector is displayed.
 155 Black dashed lines in panels a and b indicate the line across which the zonal wind changes
 156 direction, referred to as “turning point” in the text; arrows indicate the direction of the equatorial
 157 wind component.



158

159 **Figure 3:** Horizontal distributions of interface displacement η^* (m) and anomalies of the
 160 Eulerian tracer field ΔT (K) for the average wind forcing of the period July-September of the
 161 years a) 2019 and b) 2009. Panels c and d show the results for the same wind fields but with use
 162 of Rayleigh damping near the equator, which filters out equatorial wave disturbances. Small
 163 arrows represent flow velocity (every 10th vector is displayed). White arrows highlight key
 164 currents.

165 3 Results and discussion

166 There is a high similarity of the average July-September wind fields between the years of
 167 2009 and 2019 (**Figure 2**). The general feature of the wind pattern for the period July-September
 168 is that southeasterly wind found south of the equator turns into southwesterly wind north of the

169 equator. However, there is a slight but important difference between the years, discussed in the
170 following. For this purpose, we define the “turning point” as the contour line that marks the
171 directional change of the zonal wind component U , defined by $U = 0$. In 2019, the turning point
172 was located north of the equator in the region east from 96°E, where it established equatorial
173 wind with an easterly component (Fig. 2a). In contrast, in 2009, the turning point was located
174 100-200 km south of the equator; that is, the equatorial wind had a westerly component (Fig. 2c).
175 Hence, there is a distinct reversal of the direction of the equatorial wind component, noting that
176 equatorial wind-stress magnitudes are generally low (0.01-0.04 Pa). The upwelling-favorable
177 wind along Sumatra intensified in 2019, also reported by Lu and Ren (2020), which shows up as
178 anomalies in both wind-stress components (Fig. 3e-f). Wind anomalies along Java’s south coast
179 are relatively small.

180 It is interesting to note that a slight northwestward displacement by ~100-200 km of the
181 average wind field (represented by 2009 data) would largely replicate key features of the wind
182 field characterizing the 2019 pIOD event.

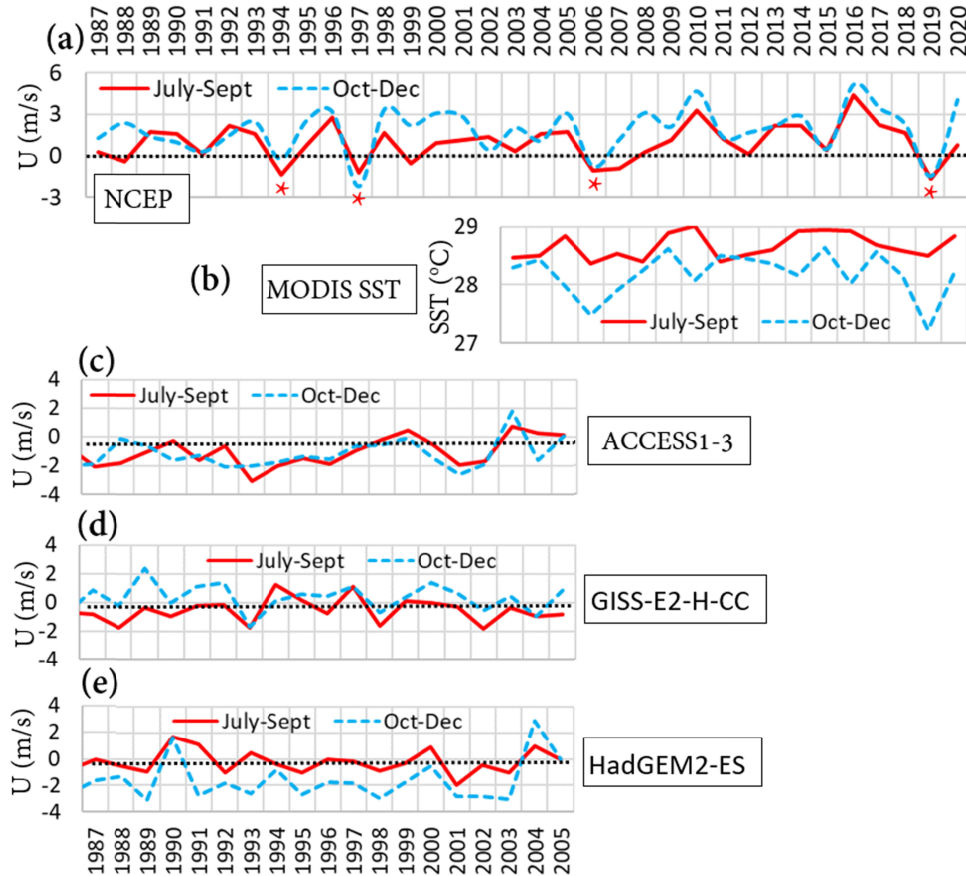
183 The wind forcing of 2019 creates pronounced upwelling along the south coast of Java and
184 the southwest coast of Sumatra with the vertical displacement of the thermocline exceeding 50 m
185 after 60 days of simulation (**Figure 3a**). This upwelling is the agent to lower SSTs in waters up
186 to ~200 km from the coast. Via the geostrophic adjustment process, the upwelling process
187 creates dynamic pressure anomalies that lead to the formation of a northwestward flow, which is
188 a classical upwelling jet (see Kämpf and Chapman, 2016). This flow, attaining a speed of 50
189 cm/s in the simulation, strongly resembles the structure of the observed South-East Sumatra
190 Current (SESC) (Kämpf and Kavi, 2019). The advective deformation of the model’s Eulerian
191 tracer field demonstrates that the flow operates to displace colder surface water northward (Fig.
192 3a, lower panel). The predicted SST anomalies agree with observational evidence both in terms
193 of magnitude and location (see Kämpf and Kavi, 2019). The zone of advective SST anomalies is
194 located adjacent to the zone of coastal upwelling, hence effectively enlarging the zone of
195 negative SST anomalies in the region. From this it can be concluded that advective effects play
196 an important role in the development of pIOD events.

197 Note that the 2019 wind field does not induce significant thermocline variations along the
198 equator. This implies that a downwelling effects along the equator cancel the upwelling due to
199 the lee effect.

200 The slightly different wind field of 2009 produces vastly different results (**Figure 3b**).
201 Here the wind forcing induces downwelling in a broad zone along the equator extending along
202 the coastlines of Sumatra and Java. Downward displacements of the thermocline are ~50 m.
203 Geostrophic adjustment of the dynamic pressure field creates a southeastward surface flow,
204 resembling the extension of the Equatorial Current (see Kämpf and Kavi, 2019). This surface
205 flow operates to transport warmer, tropical water southeastward along Sumatra’s coast. It is
206 obvious that the deepening of the thermocline along Sumatra’s and Java’s coasts supersedes the
207 effect of upwelling-favorable coastal winds. A downwelling coastal Kelvin wave initiated along
208 the equator is the principal cause of this thermocline deepening.

209 The dominant effect of equatorial winds on IOD events becomes more apparent with the
210 use of a Rayleigh damping zone that filters away flow divergences along the equator. Here, the

211 wind fields of the years 2009 and 2019 produce similar results characterized by coastal
 212 upwelling along the coasts of Java and Sumatra, and the formation of a northwestward upwelling
 213 jet (**Figure 3c-d**). There is a slight enhanced of the upwelling in 2019, which is explained by the
 214 intensification of coastal winds (see Fig. 2). These findings indirectly prove that slight changes in
 215 equatorial winds control the development of pIOD events.



216

217 **Figure 4:** Time series for the periods of July-September (red full line) and October-December
 218 (blue broken line) of a) average zonal equatorial wind speed U (m/s) between 80°E and 100°E
 219 using NCEP reanalysis data, and b) SSTs for the region (90°E - 100°E , 5° - 0°) using MODIS SST
 220 data. Panels c) to e) are the same as panel a) but show selected historical CMIP5 climate model
 221 results. Red asterisks in panel a) highlight pIOD events.

222 Observed zonal wind speeds between 80°E and 100°E along the equator for July-
 223 September confirm that, while a westerly wind component is a typical feature for most years,
 224 pIOD events stand out by the existence of an easterly wind component (**Figure 4a**). In the pIOD
 225 seasons of 1997, 2006 and 2019, easterly wind components prevail into austral spring (October-
 226 December). The analysis by Kavi and Kämpf (2022) showed that average westerly equatorial
 227 wind components follow from subsequent westerly wind bursts associated with the formation of
 228 SETIO cyclones, noting that four cyclones formed during the IOD season of 2009, whereas only
 229 a single cyclone formed in 2019. For the period July-September, surface waters of the SETIO do
 230 not display significant SST variability within 500 km from the equator (**Figure 4b**). During this
 231 period, negative SST anomalies develop farther south (see Kämpf and Kavi, 2019). This

232 indicates SST anomalies near the equator are not involved in the observed variability of the
233 equatorial zonal wind that initiates pIOD events. Consistent with this timing of events, negative
234 SST anomalies develop delayed near the equator during October-December (see Fig. 4b).

235 The accurate simulation of IOD variability is a challenging issue for climate models (Luo
236 et al., 2005; Song et al., 2008; Zhao & Hendon, 2009), which is verified here with inspection of
237 historical model results of selected CMIP5 climate models with a focus on the zonal equatorial
238 wind in the eastern Indian Ocean. While some models reproduced pIOD-like easterly wind
239 conditions, such as GISS model for 1993, overall, climate model predictions of zonal equatorial
240 winds do not agree well with observational evidence. Given the strong causal link between
241 equatorial winds and pIOD events, demonstrated here, the predictability of IOD events by
242 climate models is questionable.

243 **4 Conclusions**

244 Using a simple reduced-gravity modelling approach, this work revealed that zonal wind
245 anomalies along the equator are pivotal in the formation or suppression of positive phases of the
246 IOD, rather than coastal wind anomalies, previously suggested by Kämpf and Kavi (2019) and
247 Lu and Ren (2020). Moreover, these equatorial wind anomalies develop during austral winter
248 (July-September) in the absence of noticeable SST anomalies within 500 km from the equator.
249 This indicates that the Bjerknes feedback is not derived involved in the initial development of
250 pIODS events. Instead, it seems more plausible that the subtle change in equatorial wind
251 conditions driving IOD variability is due to large-scale drivers such as the interhemispheric sea-
252 level pressure gradient between Australia and the South China Sea/Philippine Sea, as proposed
253 by Lu and Ren (2020). Findings of the present work has important ramifications for future
254 climate research and the assessment of the performance of climate models.

255 **Acknowledgments**

256 The author does have any real or perceived financial conflicts or conflicts of interests associated
257 with this work. This work did not receive external funding. I thank Ankit Kavi for the
258 preparation of daily wind fields.

260 **Open Research**

261 All data used in this project are publicly available. CCMP V-2.0 vector wind analyses can be
262 downloaded at <http://www.remss.com/measurements/ccmp/>. NCEP-NCAR reanalysis data can
263 be downloaded at <https://www.esrl.noaa.gov/psd/data/gridded/data.ncep.reanalysis.html>. SST
264 data are taken from Aqua MODIS Global Mapped 4 μ m Nighttime Sea Surface Temperature
265 (SST4) Data, version R2019.0, that can be accessed at NASA's Giovanni data interface
266 (<https://giovanni.gsfc.nasa.gov/giovanni/>). CMIP5 climate model data are available at
267 <http://apdrc.soest.hawaii.edu/las/v6/dataset?catitem=3588>. This work used the data products of
268 "ACCESS1-3_r1i1p1 eastward near-surface wind", "GISS-E2-H_r1i1p1 eastward near-surface
269 wind" and "HadGEM2-ES_r1i1p1 eastward near-surface wind". The Fortran model code
270 including forcing data will be deposited to a FAIR compliant repository at acceptance.

271

272 **References**

- 273
- 274 Behera, S. K., Luo, J., Masson, S., Delecluse, P., Gualdi, S., Navarra, A., & Yamagata, T.
275 (2005). Paramount impact of the Indian Ocean dipole on the east African short rains: a CGCM
276 study. *Journal of Climate*, 18(21), 4514–4530. doi:10.1175/jcli3541.1
- 277
- 278 Bjerknes, J. (1966). A possible response of the atmospheric Hadley circulation to equatorial
279 anomalies of ocean temperature. *Tellus*, 18(4), 820–829. doi:10.3402/tellusa.v18i4.9712
- 280
- 281 Bjerknes, J. (1969). Atmospheric teleconnections from the equatorial Pacific. *Monthly Weather*
282 *Review*, 97(3), 163–172. doi:10.1175/1520-0493(1969)097h0163:ATFTEPi2.3.CO;2
- 283
- 284 Cai, W., Cowan, T., & Sullivan, A. (2009). Recent unprecedented skewness towards positive
285 Indian Ocean dipole occurrences and its impact on Australian rainfall. *Geophysical Research*
286 *Letters*, 36(11), 1–4. doi:10.1029/2009gl037604
- 287
- 288 Cai, W., Santoso, A., Wang, G., Weller, E., Wu, L., Ashok, K., Masumoto, Y., Yamagata, T.
289 (2014). Increased frequency of extreme Indian Ocean Dipole events due to greenhouse warming.
290 *Nature*, 510, 254–258. doi:10.1038/nature13327
- 291
- 292 Cai, W., Wang, G., Gan, B., Wu, L., Santoso, A., Lin, X., Chen, Z., Jia, F., & Yamagata, T.
293 (2018). Stabilised frequency of extreme positive Indian Ocean Dipole under 1.5 °C warming.
294 *Nature Communications*, 9(1), 1419. doi:10.1038/s41467-018-03789-6
- 295
- 296 Chan, S. C., Behera, S. K., & Yamagata, T. (2008). Indian Ocean Dipole influence on south
297 American rainfall. *Geophysical Research Letters*, 35(14), 1–5. doi:10.1029/2008gl034204
- 298
- 299 Feng, M., & Meyers, G. (2003). Interannual variability in the tropical Indian Ocean: a two-year
300 timescale of Indian Ocean Dipole. *Deep Sea Research – II. Topical Studies in Oceanography*,
301 50(12–13), 2263–2284. doi:10.1016/S0967-0645(03)00056-0
- 302
- 303 Hela, I. (1976). Vertical velocity of the upwelling in the sea. *Societas Scientiarum Fennica*, 46,
304 9–24.
- 305
- 306 Kämpf, J. (2009). *Ocean modelling for beginners: using open-source software*. Berlin: Springer
- 307
- 308 Kämpf, J. (2015). Interference of wind-driven and pressure gradient-driven flows in shallow
309 homogeneous water bodies. *Ocean Dynamics*, 65, 1399–1410. doi:10.1007/s10236-015-0882-2
- 310
- 311 Kämpf, J., & Chapman, P. (2016). *Upwelling systems of the world. A scientific journey to the*
312 *most productive marine ecosystems*. New York: Springer International Publishing.
313 doi:10.1007/978-3-319-42524-5
- 314
- 315 Kämpf, J., & Kavi, A. (2019). SST variability in the eastern intertropical Indian Ocean – On the
316 search for trigger mechanisms of IOD events. *Deep Sea Research – II. Topical Studies in*
317 *Oceanography*, 166, 64–74. doi:10.1016/j.dsr2.2018.11.010

- 318
319 Kavi, A., & Kämpf, J. (2022). Synoptic-scale atmospheric cyclones in the South-East Tropical
320 Indian Ocean (SETIO) and their relation to IOD variability. *Journal of Southern Hemisphere*
321 *Earth Systems Science*, 72, 191–201. doi:10.1071/ES22020
322
- 323 Li, T., Wang, B., Chang, C. P., & Zhang, Y. S. (2003). A theory for the Indian Ocean dipole–
324 zonal mode. *Journal of the Atmospheric Sciences*, 60(17), 2119–2135. doi:10.1175/1520-
325 0469(2003)060<2119:ATFTIO>2.0.CO;2
326
- 327 Moihamette, F., Pokam, W. M., Diallo, I., & Washington, R. (2022). Extreme Indian Ocean
328 dipole and rainfall variability over Central Africa. *International Journal of Climatology*, 42(10),
329 5255– 5272. doi:10.1002/joc.7531
330
- 331 McPhaden, M. J. (1999). Genesis and evolution of the 1997–98 El Niño. *Science*, 283, 950–954.
332 doi:10.1126/science.283.5404.950
333
- 334 Qiu, Y., Cai, W., Guo, X., & Ng, B. (2014). The asymmetric influence of the positive and
335 negative IOD events on China's rainfall. *Scientific Reports*, 4(1), 1–6. doi:10.1038/srep04943
336
- 337 Saji, N. H., Goswami, B. N., Vinayachandran, P. N., & Yamagata, T. (1999). A dipole mode in
338 the tropical Indian Ocean. *Nature*, 401(6751), 360–363. doi:10.1038/43854
339
- 340 Saji, N. H., & Yamagata, T. (2003). Possible impacts of Indian Ocean dipole mode events on
341 global climate. *Climate Research*, 25, 151–169. doi:10.3354/cr025151
342
- 343 Webster, P. J., Moore, A. M., Loschnigg, J. P., & Leben, R. (1999). Coupled ocean-atmosphere
344 dynamics in the Indian Ocean during 1997–98. *Nature*, 401, 356–359. doi.org/10.1038/43848